ceramics

MDPI

Article

Water-Based Yttria-Stabilized Nano-Zirconia Pastes for Direct Ink Writing of Dental Structures

Panagiota Angelopoulou [1], Eleni Roussi [1], Paraskevi Gkomoza [1], Michaela Papageorgiou [1], Olga Alexiadou [1], Savvas Koltsakidis [2], Dimitris Tzetzis [2], Constantina-Dia Andreouli [3], Athena Tsetsekou [1,†] and Ioanna Kitsou [1,*]

[1] School of Mining and Metallurgical Engineering, National Technical University of Athens, 15780 Athens, Greece; p.angelopoulou@gmail.com (P.A.); elerou@metal.ntua.gr (E.R.); pgomoza@metal.ntua.gr (P.G.); michaelap@mail.ntua.gr (M.P.); oalexiadou@metal.ntua.gr (O.A.); athtse@metal.ntua.gr (A.T.)
[2] Digital Manufacturing and Materials Characterization Laboratory, School of Science and Technology, International Hellenic University, 57001 Thessaloniki, Greece; skoltsakidis@ihu.edu.gr (S.K.); d.tzetzis@ihu.edu.gr (D.T.)
[3] Materials Industrial Research and Technology Center S.A., Research & Development Directorate, 76 km Athens-Lamia national Road, 32009 Schimatari, Greece; d.andreouli@mirtec.gr
* Correspondence: kitioanna@metal.ntua.gr; Tel./Fax: +30-210-7722179
† Deceased author.

Abstract

In this work, zirconia ceramic structures were fabricated by Direct Ink Writing (DIW) using water-based, yttria-stabilized nano-zirconia pastes. The pastes were prepared from 3 mol% yttria-stabilized zirconia nanopowders synthesized by sol–gel and co-precipitation routes. The effects of dispersant concentration and organic additives on paste preparation and printability were investigated, and the rheological behavior of the printable formulations was evaluated. The microstructure of the sintered 3D-printed specimens was examined by scanning electron microscopy (SEM), while apparent porosity, density, and compressive strength were determined. All printable pastes exhibited shear-thinning behavior. After sintering at 1500 °C, the printed specimens showed submicron grain sizes and apparent porosities as low as 3%. The formulation prepared without acrylamide and crosslinking agent (O12X) exhibited an apparent porosity of 3% and a compressive strength of 350 ± 25 MPa. The co-precipitated-powder formulation (2N) reached compressive-strength values of up to 360 ± 25 MPa. These results demonstrate the feasibility of using high-solids, water-based nano-zirconia pastes for DIW fabrication of dense zirconia structures and support further investigation of this approach for dental applications.

Keywords: bioceramics; yttria-stabilized zirconia; direct ink writing; additive manufacturing; 3D printing; aqueous ceramic paste

Check for updates

Academic Editors: Bartolomeo Coppola, Frank Kern and Julien Schmitt

Received: 22 September 2026
Revised: 2 October 2026
Accepted: 5 October 2026
Published: 8 October 2026

Copyright: © 2026 by the authors. Licensee MDPI, Basel, Switzerland. This article is an open access article distributed under the terms and conditions of the Creative Commons Attribution (CC BY) license.

1. Introduction

Recent advances in materials science have led to substantial developments in dental implants and prosthetic restorations. Metallic implants and prosthetic components, including abutments, are commonly manufactured from titanium and titanium alloys. Although these materials exhibit favorable mechanical properties, biocompatibility, and osseointegration, metallic components may be associated with hypersensitivity reactions in susceptible individuals and may compromise esthetics in the anterior region, particularly in patients with thin peri-implant mucosa [1,2]. These considerations have encouraged

the development of metal-free ceramic alternatives. Among the ceramics used for dental restorations, alumina-toughened zirconia and yttria-stabilized zirconia are of particular interest [3].

Zirconia is a biocompatible ceramic with mechanical properties suitable for a range of dental applications. It exhibits high corrosion resistance, chemical stability, and favorable biological responses, while its white color can provide an esthetic advantage over metallic components. A key limitation is its brittle nature. Pure zirconia undergoes reversible monoclinic-to-tetragonal and tetragonal-to-cubic phase transformations as temperature increases. Stabilizing oxides, most commonly yttria, are therefore added to retain metastable tetragonal zirconia at room temperature and improve mechanical performance. The yttria content affects the phase assemblage and, consequently, the optical and mechanical properties, increasing yttria content generally improves translucency but can reduce mechanical performance [4–9]. Thus, selection of zirconia compositions for dental restorations requires balancing mechanical, optical, and biological requirements.

Conventional fabrication of zirconia dental restorations commonly relies on subtractive manufacturing by milling or grinding using computer-aided design/computer-aided manufacturing (CAD/CAM) workflows. These approaches can generate substantial material waste and may present challenges when complex geometries are required [10,11]. Additive manufacturing (AM), or 3D printing, provides an alternative route in which components are built layer by layer.

Additive manufacturing is increasingly investigated for the fabrication of bioceramic components [12–15]. Although questions remain regarding the long-term mechanical and esthetic performance of additively manufactured zirconia restorations, recent studies have reported promising results. Studies examining tribological behavior under simulated mastication and the interaction of 3D-printed zirconia with antagonist natural teeth have shown that additively manufactured specimens may exhibit lower hardness than subtractively manufactured counterparts, while wear behavior can remain comparable [16,17]. AM therefore represents a promising route for zirconia dental components. However, the properties of printed ceramics, including porosity and dimensional stability, depend strongly on the feedstock formulation and processing conditions [18]. Nanostructured powders and pastes can provide useful control over these factors.

Direct Ink Writing (DIW), also referred to as robocasting in ceramic processing, requires inks with rheological properties that allow extrusion through a nozzle while maintaining the geometry of the deposited filament. Teegen et al. [19] reported satisfactory mechanical properties for DIW-printed zirconia/yttria-containing specimens compared with conventionally processed materials. Previous studies have demonstrated the feasibility of DIW/robocasting of yttria-stabilized zirconia using aqueous, high-solids formulations, including binder-free systems and formulations intended for dental applications [20–23]. Comparatively less attention has been given to the use of laboratory-synthesized 3Y-ZrO_2 nanopowders obtained through different wet-chemical synthesis routes within the same aqueous DIW processing framework. This provides the motivation for the present comparison of sol–gel- and co-precipitation-derived nanopowders and their corresponding printable formulations. Accordingly, the contribution of this study lies in the comparative processing of two laboratory-synthesized 3Y-ZrO_2 nanopowders within an aqueous DIW framework, together with the evaluation of a formulation without acrylamide and crosslinking agent.

In the present study, laboratory-synthesized 3 mol% yttria-stabilized zirconia nanopowders with narrow particle-size distributions were used to formulate water-based pastes for DIW. Formulations with and without organic additives were examined. The objective was to evaluate the influence of powder route, dispersant concentration, solids

loading, and additives on paste processing, printability, sintered microstructure, apparent porosity, and compressive strength. Particular attention was given to the feasibility of a formulation without acrylamide and crosslinking agent, with the longer-term aim of developing zirconia structures for dental applications.

2. Materials and Methods

2.1. Synthesis and Characterization of Yttria Stabilized Zirconia Nanopowders

Two wet-chemical routes were used to obtain yttria-stabilized zirconia nanopowders: sol–gel (3YZrO$_2$-O) and co-precipitation (3YZrO$_2$-N). The procedures were adapted from Tyagi et al. [24], with the addition of 3 mol% yttria. For the sol–gel route, zirconium (IV) propoxide (70% in propanol, Acros Organics, Geel, Belgium) and yttrium nitrate hexahydrate (Alfa Aesar, Karlsruhe, Germany) were used at a ZrO_2:$Y2O_3$ molar ratio of 0.97:0.03 and dissolved in n-propanol. Ammonia solution (25%, Carlo Erba, Val-de-Reuil, France) was added dropwise until pH 10.5 was reached. The resulting gel was aged for 1 h, dried at 110 °C for 12 h, and calcined at 600 °C for 4 h. For the co-precipitation route, zirconyl nitrate hydrate (Thermo Scientific, Waltham, MA, USA) was used as the zirconia precursor and distilled water as the solvent. Ammonia solution (25%, Carlo Erba) was added dropwise until pH 10.5 was reached. The resulting suspension was stirred for 24 h, collected, washed several times with water, dried at 110 °C for 12 h, and calcined at 500 °C for 4 h. The co-precipitated nanopowder was subsequently subjected to high-energy ball milling for 15 min at 300 rpm to reduce agglomeration. Powder morphology and primary particle size were examined using high-resolution transmission electron microscopy (HRTEM, JEOL 2100 HR, JEOL Ltd., Akishima, Tokyo, Japan), and crystallinity was assessed by X-ray diffraction (XRD, Bruker D8 Focus, Bruker AXS GmbH, Karlsruhe, Germany) using Ni-filtered Cu Kα radiation (λ = 1.5406 Å) at 40 kV and 40 mA over a 2θ range of 20–80°. Crystallite size was estimated from the diffraction peaks using the Scherrer equation:

$$D = \frac{K\lambda}{\beta cos\theta}$$

where:

D is the crystallite size (in nanometers),
K is the Scherrer constant (here set to 0.9),
λ is the wavelength of the X-ray source,
β is the full width at half maximum (FWHM),
θ is the peak position (in radians).

This formula allows the calculation of the crystallite size based on the X-ray diffraction data.

For the 3YZrO$_2$-N powder, quantitative phase analysis was additionally performed by Rietveld refinement of the XRD pattern using GSAS-II software 5841/v5.8.2., considering tetragonal and monoclinic ZrO_2 phases. The relative phase fractions were determined from the refined scale factors.

2.2. Nano-Zirconia Feedstock Preparation and Characterization

To prepare the nano-zirconia feedstock, the nanopowders were wet ball-milled with aqueous solutions of the dispersant Dolapix CE64 (Zschimmer & Schwarz, Lahnstein, Germany) to promote deagglomeration and obtain homogeneous suspensions. Different Dolapix CE64 concentrations, expressed as wt.% relative to the zirconia powder, were mixed with distilled water and ball-milled for 24 h. The viscosity of each slurry was then measured using a Rotavisc Lo-Vi viscometer (IKA-Werke GmbH & Co. KG, Staufen, Germany) to

identify the dispersant concentration associated with the minimum viscosity. The treated nanopowders were subsequently collected and freeze-dried before paste preparation.

Printable pastes were prepared in a mechanical vacuum stirrer (Vacuret, Reitel, Germany) by mixing the powder with acrylamide (Thermo Fisher Scientific) as monomer, N,N′-methylenebisacrylamide (Alfa Aesar) as crosslinking agent, and distilled water, for 15 min at 320 rpm to obtain homogeneous pastes. A broader formulation study was conducted to evaluate solids loading and additive content; however, only the successfully printed formulations are reported here. Pastes containing 66–78 wt.% solids were prepared from 3YZrO$_2$-O, whereas 3YZrO$_2$-N formulations contained 80–88.5 wt.% solids. For comparison, a 3YZrO$_2$-O paste without acrylamide or crosslinking agent (O12X), but containing dispersant, was prepared at 74 wt.% solids (Table 1). An analogous additive-free paste based on 3YZrO$_2$-N could not be prepared successfully because the formulation exhibited pronounced time-dependent rheological behavior.

Table 1. Composition of the examined pastes.

Paste Code	wt.% Solids	% Dolapix CE64	% Acrylamide	% N,N′ Methylenebisacrylamide
O12	78	1.2	0.095	0.0095
O12X	74	1.2	-	-
2N	88.5	2	0.0284	0.00284

Rheological measurements were performed using an Anton Paar MCR 92 (Graz, Austria) rheometer with a 20 mm parallel-plate geometry and a 1 mm gap at room temperature. Flow ramps were conducted over shear rates of 0.01–500 s^{-1}.

2.3. 3D Printing Process and Characterization of Cuboid Samples

An Axolotl A1 Bio Printer (Axolotl Biosystems, Istanbul, Turkey) equipped with a pneumatic extrusion head was used to print the cuboid and tooth-shaped specimens. Applied pressure ranged from 0.2 to 7 bar depending on paste viscosity, and the printing speed was 15 mm/s. Several nozzle diameters and corresponding extrusion pressures were evaluated and nozzles with internal diameters of 0.8 and 1.1 mm were selected for the final printing trials. The printing parameters that were tested for each specimen are summarized in Table 2.

Table 2. 3D-printing parameters.

	Pastes		
Parameters	**O12**	**O12X**	**2N**
Nozzle diameter (mm)	1.1	1.1	0.8
Layer thickness (mm)	0.35	0.35	0.35
Speed (mm/s)	15	15	15
Air pressure (bar)	5	5	4.4

The printed green specimens were dried first at room temperature and then at 80 °C for 12 h. The dried specimens were thermally treated at 400 °C for 1 h to remove the binders and subsequently sintered at 1500 °C for either 2 or 4 h.

Linear shrinkage was determined by measuring the lateral dimensions of the cuboid specimens (n = 5) before and after sintering using a caliper. As the specimens had a square cross-section and comparable shrinkage was observed along both lateral directions, the dimensional change was expressed as linear shrinkage. Linear shrinkage was calculated according to:

$$\text{Linear shrinkage (\%)} = [(L_0 - L_s)/L_0] \times 100 \quad (1)$$

where L_0 is the initial lateral dimension of the green specimen and L_s is the corresponding dimension after sintering. No measurable variability was observed among the specimens within the resolution of the dimensional measurements; therefore, shrinkage is reported as a single representative value.

Fracture-surface morphology and grain size were examined using scanning electron microscopy (SEM, JEOL 6380LV, JEOL Ltd., Akishima, Tokyo, Japan). The grain size was measured directly from the SEM images using ImageJ (version 1.54g, National Institutes of Health, Bethesda, MD, USA) image analysis software. The mean grain size and standard deviation were calculated from measurements of 50 individual grains for each material and sintering condition. Bulk density and apparent porosity were determined by the Archimedes method following the procedure described in the cited ASTM standard [25]. Specimens (n = 5 per formulation) were dried to constant mass at 105–110 °C and the dry mass (D) was recorded. They were then immersed in water, boiled for 2 h, cooled while submerged, and maintained in water for at least 12 h. The suspended mass in water (S) and saturated mass in air (W) were subsequently recorded. Exterior volume, apparent porosity, and bulk density were calculated using Equations (2)–(4).

$$V = W - S \text{ (in } cm^3) \quad (2)$$

$$\%P = [(W - D)/V] \times 100 \quad (3)$$

$$B = D/V \text{ (in } gr/cm^3) \quad (4)$$

Compressive strength was measured using an Instron 4482 testing machine at room temperature (20 ± 2 °C) and a crosshead speed of 1 mm/min. Five sintered cubic specimens were tested for each reported condition. Prior to testing, the actual dimensions of each sintered specimen were measured, and the corresponding loaded cross-sectional area was calculated. Compressive strength (σ) was determined from the maximum load at failure according to:

$$\sigma = F_{max}/A \quad (5)$$

where F_{max} is the maximum load at failure and A is the actual loaded cross-sectional area of the sintered specimen. The mean compressive strength and standard deviation were subsequently calculated for each condition.

3. Results

3.1. Zirconia Nanopowders

XRD analysis showed that both calcined nanopowders were crystalline and predominantly tetragonal (Figure 1e). The main reflections were observed at 2θ ≈ 30.1°, 34.9°, 50.3°, 60.0°, 62.5°, and 74.3°, corresponding to the (111), (200), (220), (311), (222), and (400) planes of tetragonal zirconia (JCPDS No. 14-0534). A minor monoclinic contribution was detected only for 3YZrO$_2$-N, with a peak at 2θ ≈ 28.1° assigned to the (−111) plane (JCPDS No. 37-1484) [26]. Quantitative phase analysis by Rietveld refinement indicated approximately 87.1 wt.% tetragonal ZrO_2 and 12.9 wt.% monoclinic ZrO_2 for 3YZrO$_2$-N (Figure S1). The final refinement yielded R_w = 13.43% and a reduced χ^2 of 1.401. Transmission electron microscopy confirmed the nanostructured morphology, and the corresponding SAED patterns were consistent with crystalline zirconia (Figure 1a–d). Mean primary particle sizes of approximately 10 nm for 3YZrO$_2$-N and 12 nm for 3YZrO$_2$-O were observed, together with agglomerates of approximately 100–200 nm. Scherrer analysis of the peak at 2θ ≈ 30.1° yielded crystallite sizes of 9.02 nm for 3YZrO$_2$-N and 9.9 nm for 3YZrO$_2$-O.

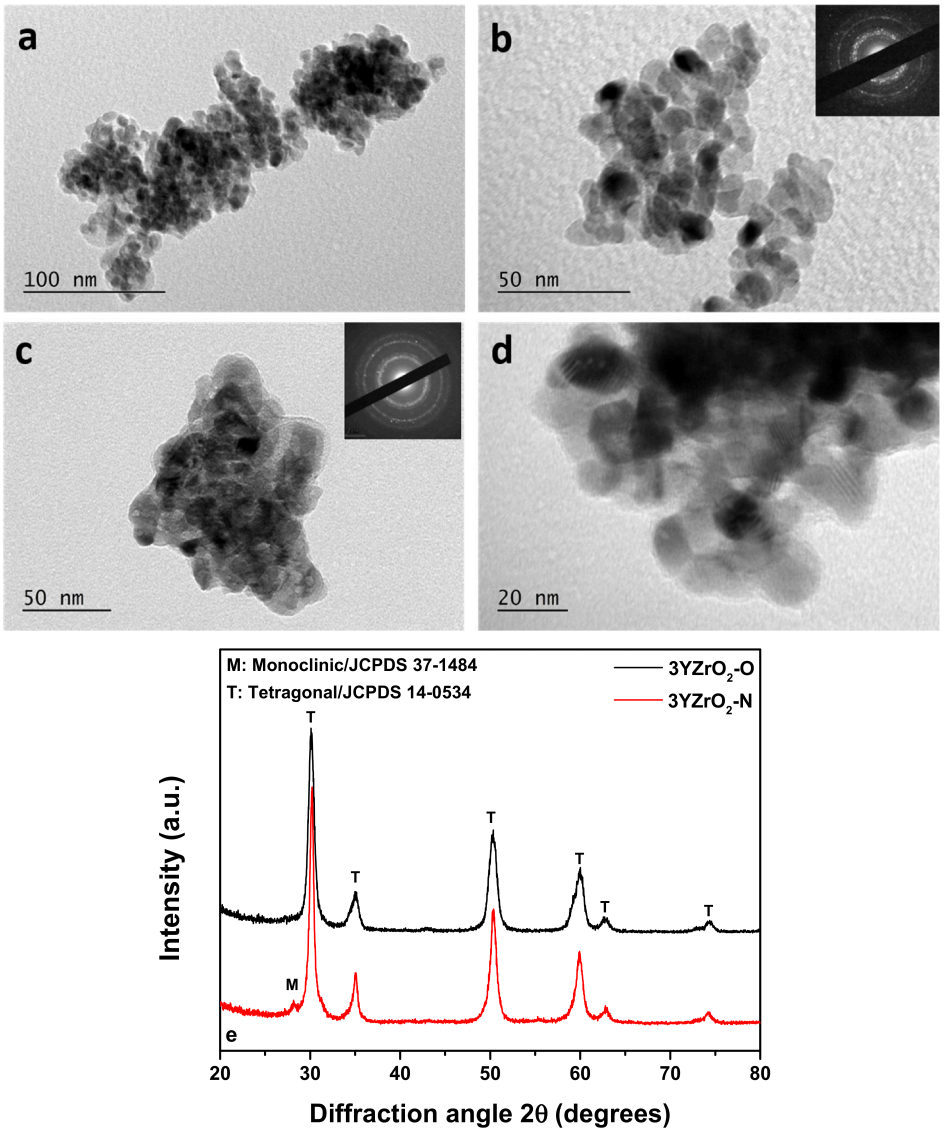


Figure 1. TEM images of $3YZrO_2$-N (**a**,**b**) and $3YZrO_2$-O (**c**,**d**) and their respective X-Ray diffraction patterns (**e**).

To optimize deagglomeration, 50 wt.% aqueous zirconia slurries containing 0.5–4 wt.% dispersant relative to powder mass were wet ball-milled and their viscosity was measured. As shown in Figure 2a, increasing the Dolapix CE64 concentration initially reduced the viscosity, reaching minima of 5.64 mPa·s for $3YZrO_2$-O at 1.2 wt.% dispersant and 3.46 mPa·s for $3YZrO_2$-N at 2 wt.% dispersant. Further increases in dispersant concentration resulted in higher viscosity. Accordingly, 1.2 wt.% Dolapix CE64 for $3YZrO_2$-O and 2 wt.% for 3YZrO2-N were selected for subsequent paste preparation. Following wet ball milling, the powders were collected and freeze-dried.

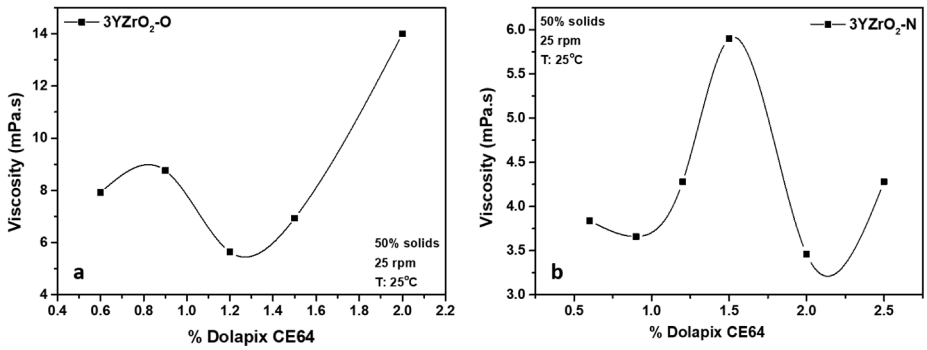


Figure 2. Effect of dispersant concentration (wt.% relative to powder mass) on slurry viscosity for 3YZrO$_2$-O (**a**) and 3Y-ZrO$_2$-N (**b**).

3.2. Zirconia Pastes

A broader formulation study evaluated solids loading and additive concentration, although only the successfully printed pastes are reported here. Formulations containing 66–78 wt.% solids for 3YZrO$_2$-O and 80–88.5 wt.% solids for 3YZrO$_2$-N were prepared. The best shape retention and printing quality were obtained at the highest solids loading within each powder series. Lower-solids formulations showed deformation, insufficient shape retention, and/or geometric printing defects. The selected 2N and O12 pastes therefore contained 88.5 and 78 wt.% solids, respectively.

All three printable pastes exhibited shear-thinning behavior, with viscosity decreasing as shear rate increased (Figure 3), which facilitates extrusion under applied shear. However, rheological suitability for DIW cannot be fully assessed from viscosity–shear rate measurements alone. O12 and O12X exhibited higher viscosities at low shear rates than 2N. Accordingly, O12 and O12X were printed using a 1.1 mm internal-diameter nozzle, whereas a 0.8 mm nozzle was used for 2N. O12 also showed higher viscosity than O12X. Because these formulations differed in both solids loading and additive composition, the present data do not allow the contribution of the organic additives to viscosity to be isolated independently.

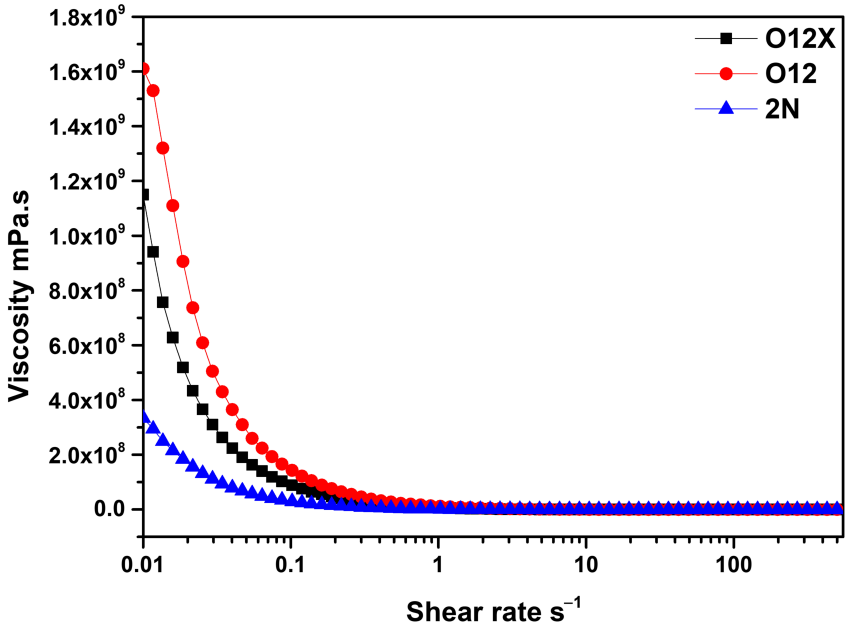


Figure 3. Viscosity of the printable pastes as a function of shear rate.

3.3. 3D-Printed Cuboid Samples

Cuboids of 10 mm × 10 mm × 10 mm as well as teeth structures were 3D-printed utilizing the pastes described earlier (Figure 4). The tooth-shaped specimens shown in Figure 4 are presented as a qualitative feasibility demonstration of the ability of the developed pastes to print more complex dental-like geometries. Dimensional accuracy was not evaluated in the present study.

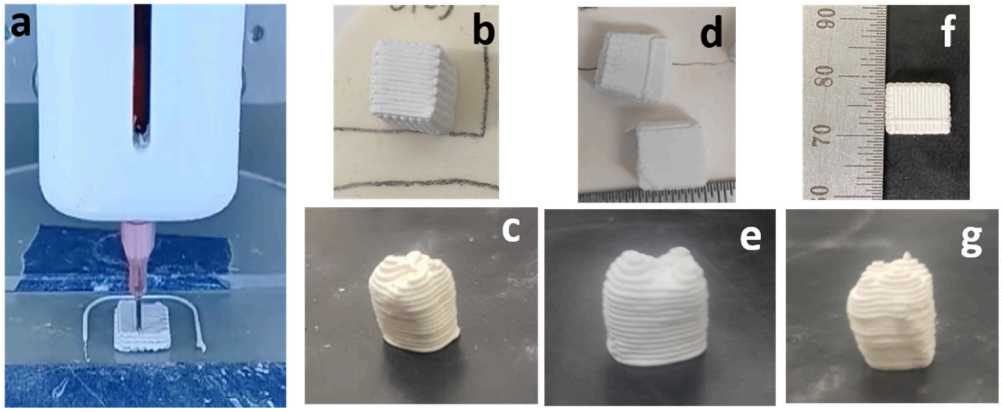


Figure 4. Representative image of the DIW printing process (**a**) and optical images of the green printed cuboids and tooth-shaped specimens: O12 (**b**,**c**), O12X (**d**,**e**), and 2N (**f**,**g**). O12 specimens were dried at 80 °C for 12 h, subjected to debinding at 400 °C for 1 h, and sintered at 1500 °C for 2 or 4 h. SEM images of the sintered specimens are shown in Figure 5. Consistent with the apparent-porosity measurements (Table 3), densification increased with sintering time. Apparent porosity decreased from 19.2% after 2 h to 8% after 4 h. At the same time, average grain size increased from approximately 278 ± 80 nm to 320 ± 90 nm.

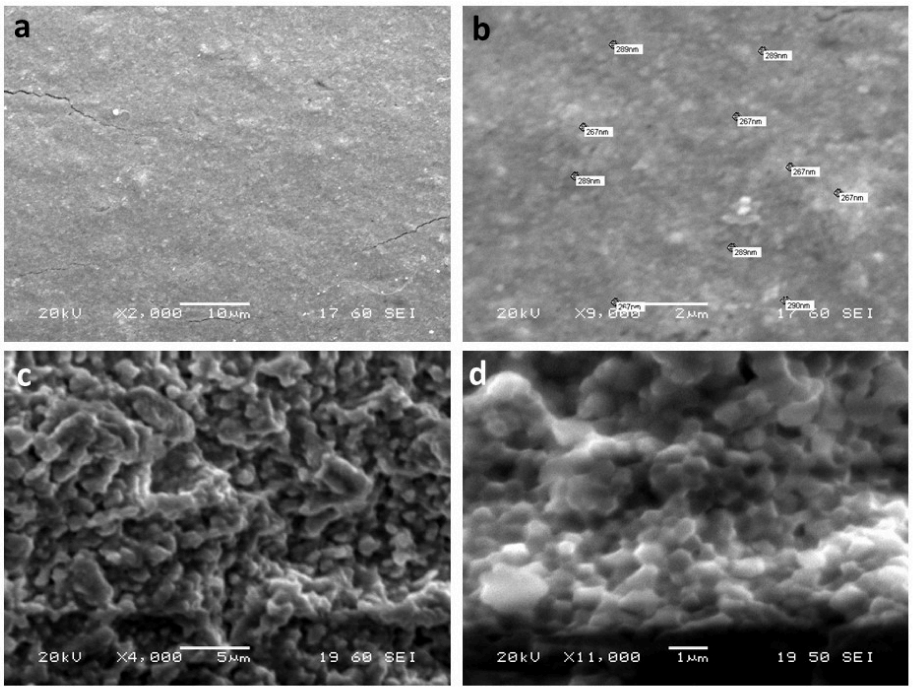


Figure 5. SEM images of O12 3D-printed cuboids after sintering at 1500 °C for 2 h (**a**,**b**) and 4 h (**c**,**d**).

Table 3. Properties of zirconia cuboids after sintering.

Specimen	Sintering					
	1500 °C 2 h			1500 °C 4 h		
	d (g/cm^3)	Apparent Porosity (%)	Compressive Strength (MPa)	d (g/cm^3)	Apparent Porosity (%)	Compressive Strength (MPa)
O12	4.54 ± 0.11	19.2 ± 0.26	75 ± 25	5.27 ± 0.05	8 ± 0.1	190 ± 20
O12X	-	-	-	5.43 ± 0.03	3 ± 0.07	350 ± 25
2N	5.1 ± 0.1	8 ± 0.11	350 ± 25	5.2 ± 0.04	6 ± 0.04	360 ± 25

Apparent porosity strongly influences the mechanical behavior of ceramic components because pores can act as stress concentrators. In the O12 series, the specimen with 19.2% apparent porosity exhibited a compressive strength of 75 ± 25 MPa, whereas the specimen sintered for 4 h, with 8% apparent porosity, reached 190 ± 20 MPa. The latter value is of the same order of magnitude as compressive-strength values reported for dental hard tissues [27]; however, direct comparison should be interpreted cautiously because specimen geometry, microstructure, and test conditions differ.

Figure 6 shows SEM images of the O12X specimen, which contained dispersant but no acrylamide or crosslinking agent. After drying and debinding, the specimen was sintered at 1500 °C for 4 h. The microstructure showed substantial densification and relatively uniform grain growth, with an average grain size of 420 ± 82 nm. O12X exhibited lower apparent porosity than O12 after 4 h at 1500 °C (3% versus 8%) and a higher compressive strength (350 ± 25 MPa versus 190 ± 20 MPa).

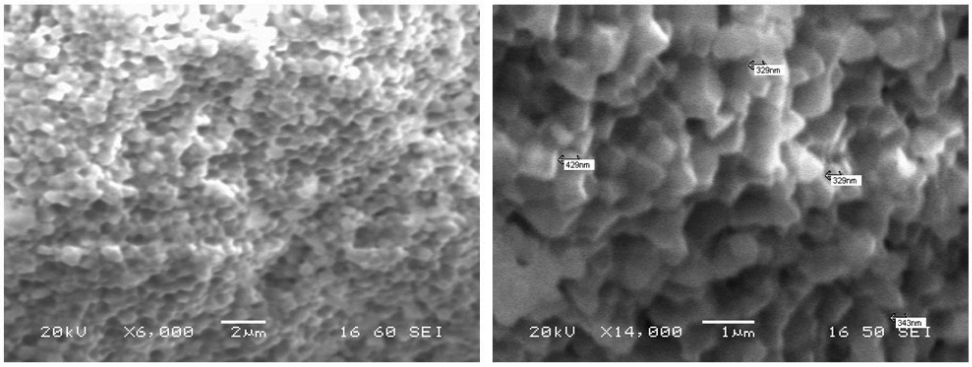


Figure 6. SEM images of O12X 3D-printed cuboids after sintering at 1500 °C for 4 h.

SEM images of the 2N specimens are shown in Figure 7. The specimens exhibited a dense microstructure with a relatively uniform submicron grain size. Average grain size increased from approximately 228 ± 102 nm to 360 ± 88 nm when the sintering time increased from 2 to 4 h. Only small changes in apparent porosity and compressive strength were observed between the specimens sintered for 2 and 4 h (Table 3). Specifically, for the first sintering cycle, these values were found to be 8% and 350 MPa, respectively, while with the increase in the sintering duration from 2 to 4 h, the values recorded were 6% and 360 MPa, respectively.

The compressive-strength values obtained for O12X and 2N are within the range of values reported for dental hard tissues [28,29]. However, this comparison is provided only as a contextual reference and should not be interpreted as evidence of equivalent mechanical or clinical performance, since the materials, specimen geometries, and testing conditions differ.

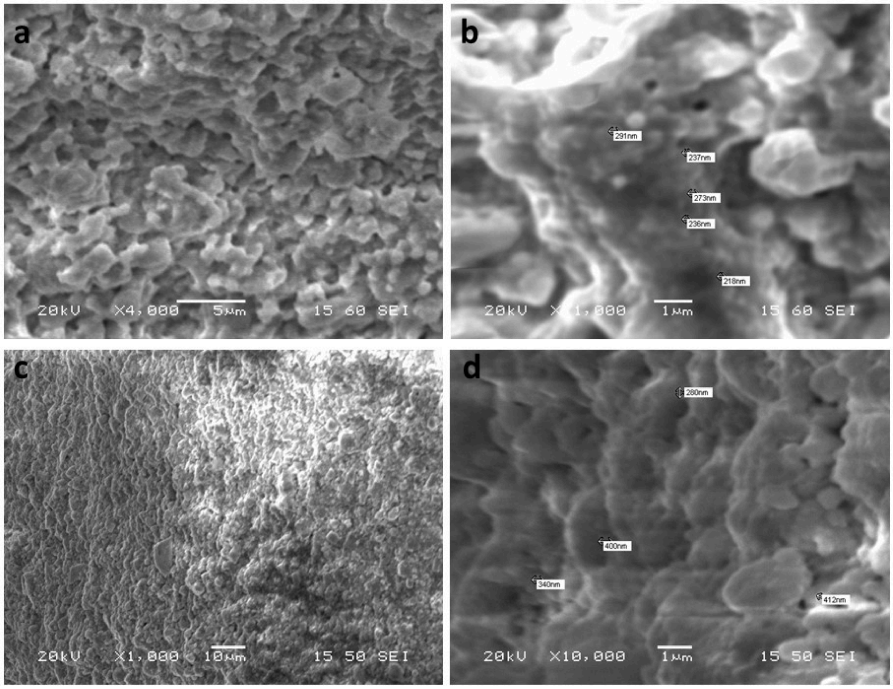


Figure 7. SEM images of 2N 3D-printed cuboids after sintering at 1500 °C for 2 h (**a**,**b**) and 4 h (**c**,**d**).

4. Discussion

Two 3Y-ZrO_2 nanopowders were successfully synthesized by sol–gel and co-precipitation routes. Nanopowders have a strong tendency to agglomerate because of their small particle size and high surface energy. Such agglomeration can adversely affect particle packing and contribute to heterogeneous densification and grain growth during sintering [30]. The dispersant-assisted wet-milling step was therefore used to reduce agglomeration before paste preparation. This treatment was intended to improve suspension homogeneity and promote a more uniform sintered microstructure.

Pastes containing 66–78 wt.% solids for 3YZrO_2-O and 80–88.5 wt.% solids for 3YZrO_2-N were prepared. The best printing quality was obtained for the formulations with the highest solids loading in each series, whereas lower-solids formulations showed deformation, poor shape retention, and/or geometric defects. All selected printable formulations exhibited shear-thinning behavior, which is advantageous for DIW because the paste must flow through the nozzle under shear while recovering sufficient resistance to deformation after deposition. The present rheological dataset establishes shear-thinning behavior but does not independently quantify yield stress, post-extrusion structural recovery, or oscillatory properties such as storage and loss moduli. These parameters would be useful in future work for a more complete assessment of printability.

The 3YZrO_2-N formulation enabled a higher solids loading than the 3YZrO_2-O formulations and exhibited a lower measured linear shrinkage after sintering (10% for 2N compared with 20% for O12 and O12X). The difference may be related, at least in part, to the different solids contents of the pastes. Reported shrinkage values for additively manufactured zirconia vary with feedstock and sintering conditions: Muccillo et al. [31] reported values of approximately 25%, Li et al. [32] reported 20.2% near 1500 °C, and Yu et al. [33] reported values up to 36.8% under higher-temperature processing. The co-precipitation route used for 3YZrO_2-N, however, required additional washing and mechanical-milling steps. Notably, O12X, which contained no acrylamide or crosslinking agent, showed the lowest apparent porosity (3%) and a compressive strength of 350 ± 25 MPa after sintering for 4 h. This result suggests that formulation without acrylamide and crosslinking agent is

worthy of further investigation. Nevertheless, O12 and O12X also differed in solids loading; therefore, the observed differences cannot be attributed solely to the absence of organic additives. Eliminating acrylamide and the crosslinking agent may simplify processing and reduce the amount of organic material removed during debinding, but the effects on defect formation and mechanical performance should be confirmed through controlled formulations with matched solids loading. Rietveld refinement further showed that the co-precipitated 3YZrO_2-N powder contained 87.1 wt.% tetragonal and 12.9 wt.% monoclinic ZrO_2. Despite this difference in the initial phase assemblage, the 2N specimens exhibited compressive-strength values of 350–360 MPa, comparable to the 350 ± 25 MPa measured for O12X. Thus, the presence of a monoclinic fraction in the starting 3YZrO_2-N powder did not prevent the development of relatively high compressive strength after sintering. However, its individual contribution cannot be isolated because the formulations also differed in solids loading and processing history, while the post-sintering phase composition was not quantified.

Because mastication includes substantial compressive loading, compressive strength provides useful initial information for assessing candidate dental materials [34]. Published data specifically addressing the compressive strength of additively manufactured zirconia remain limited. Buj-Corral et al. [35] reported 172 ± 86 MPa in preliminary testing of a low-porosity specimen, whereas Frąckiewicz et al. [36] reported substantially higher values of 4.16 ± 0.53 GPa. Such differences emphasize the sensitivity of measured compressive strength to material state, specimen geometry, processing history, and testing protocol. Chun and Lee [37] further showed that the mechanical behavior of restorative materials and dental hard tissues cannot be represented by a single property. Accordingly, the compressive-strength values measured in the present study should be considered encouraging screening results rather than direct evidence of clinical equivalence to enamel, dentin, or natural teeth.

To facilitate comparison among the investigated formulations, the main processing parameters and resulting properties are summarized in Table 4.

As summarized in Table 4, the investigated formulations show distinct combinations of solids loading, printing conditions, shrinkage, and final properties. The 2N formulation enabled the highest solids loading and exhibited the lowest linear shrinkage, whereas O12X showed the lowest apparent porosity and relatively high compressive strength. Comparison with representative literature data further illustrates the broad range of properties reported for DIW-processed zirconia and highlights the strong dependence of the final performance on feedstock formulation and processing conditions. Because several processing variables differed among the present formulations, these trends should be interpreted at the formulation level rather than attributed to a single parameter.

The literature data summarized in Table 5 illustrate the broad range of densification and mechanical properties reported for extrusion-based processing of zirconia. Relative densities approaching 99% have been achieved in high-solids aqueous systems, while the reported mechanical response varies considerably with feedstock composition, printing conditions, sintering, specimen geometry, and testing method. Of particular relevance to the present study, compressive-strength values of 172 ± 86 MPa and 1.56 GPa have been reported for extrusion-printed YSZ under substantially different processing and testing conditions [33,35]. Accordingly, the compressive-strength values of 350–360 MPa obtained for O12X and 2N should be viewed as encouraging results within this broad literature range rather than as directly equivalent material-performance values.

Table 4. Summary table.

					Sintering							
					1500 °C 2 h				1500 °C 4 h			
	Synthesis Route	**Solids (wt.%)**	**Nozzle Diameter (mm)/Pressure (bar)**	**Linear Shrinkage (%)**	**d (g/cm^3)**	**Apparent Porosity (%)**	**Compressive Strength (MPa)**	**Grain Size (nm)**	**d (g/cm^3)**	**Apparent Porosity (%)**	**Compressive Strength (MPa)**	**Grain Size (nm)**
O12	Sol–gel	78	1.1/5	20	4.54 ± 0.11	19.2 ± 0.26	75 ± 25	278 ± 80	5.27 ± 0.05	8 ± 0.1	190 ± 20	320 ± 90
O12X	Sol–gel	74	1.1/5	20	-	-	-	-	5.43 ± 0.03	3 ± 0.07	350 ± 25	420 ± 82
2N	Co-precipitation	88.5	0.8/4.4	10	5.1 ± 0.1	8 ± 0.11	350 ± 25	228 ± 102	5.2 ± 0.04	6 ± 0.04	360 ± 25	360 ± 88

Table 5. Representative literature data for DIW/robocasting of yttria-stabilized zirconia.

Material/Formulation	**Solids Loading ***	**Printing Conditions**	**Sintering Conditions**	**Key Sintered Properties**	**Mechanical Properties**	**Ref.**
YSZ, aqueous binder-free paste; 0.5 wt.% Dolapix CE64	88 wt.%	Nozzle: 450 µm	1500 °C, 2 h	RD: 97.1%	Hardness: 1485 ± 32 HV, K_{ic}: 4.11 ± 0.09 MPa.m$^{1/2}$	[20]
3YSZ aqueous paste; methylcellulose binder; DARVAN C-N dispersant	60 vol.% (~90 wt.%)	Nozzle: 1.0 mm, Speed: 60 mm/s, Pressure: 0.6 MPa	1700 °C, rapid cooling to 1550 °C, 5 h	RD: 98.1%, linear shrinkage: 36.8, 32.5, and 33.3% along the three specimen dimensions	Compressive strength: 1.56 GPa flexural strength: 488.96 ± 79.84 MPa K_{ic}: 2.63 ± 0.20 MPa·m$^{1/2}$	[33]
3Y-TZP aqueous slurry; water-soluble epoxy resin and sodium polyacrylate	58 vol.% (~89 wt.%)	Nozzle: 0.5 mm Speed: 12 mm/s pressure: 0.4–0.5 MPa	1550 °C, 2 h	RD: 99.1%	Flexural strength: 692 ± 13 MPa	[38]
3YSZ aqueous ink; Pluronic F-127; Dolapix PC75	40 vol.% (~80 wt.%)	Nozzle: 0.58 mm Speed: 3 mm/s	1550 °C	MD: 4.98 ± 0.05 g/cm^3 Shrinkage: 20.05–27.99% Total porosity: 12.36 ± 0.90%	Compressive strength: 172 ± 86 MPa	[35]
3Y-TZP aqueous ink with PEG–Laponite®	31 vol.% (~73 wt.%)	Nozzle: 0.41 mm Speed: 10 mm/s	1550 °C, 2 h	RD: 89.3 ± 0.5% Grain size: ~1 µm (m/t-ZrO_2), >5 µm (c-ZrO_2)	Hardness: 952 ± 40 HV K_{ic}: 4.6 ± 1.1 MPa·m$^{1/2}$	[39]

*K_{ic}: fracture toughness. RD: Relative Density. MD, Mean Density. * For literature formulations originally reported in vol.%, approximate wt.% equivalents were calculated assuming a zirconia density of 6.05 g cm^{-3} and a density of 1.0 g cm^{-3} for the liquid phase. These calculated values are provided only to facilitate approximate comparison with the present formulations. Mechanical-property values were obtained using different specimen geometries and testing methods and should therefore not be directly compared.*

In summary, this study demonstrates the feasibility of fabricating zirconia structures by DIW using high-solids, water-based nano-zirconia pastes. The results identify promising processing conditions and show that low apparent porosity and relatively high compressive strength can be achieved after sintering. Further work should include a more complete rheological characterization and mechanical properties directly relevant to dental restorations, including flexural strength, fracture toughness, hardness, aging behavior, and tribological performance, together with dimensional accuracy and fit assessment for crown-like geometries.

5. Conclusions

Yttria-stabilized zirconia nanopowders with mean primary particle sizes of approximately 10–12 nm were successfully produced by sol–gel and co-precipitation routes and formulated into water-based pastes for DIW. After sintering, the printed specimens exhibited submicron grain sizes and apparent porosities as low as 3%. Among the investigated formulations, O12X, prepared without acrylamide or crosslinking agent, exhibited an apparent porosity of 3% and a compressive strength of 350 $\pm$ 25 MPa after sintering at 1500 °C for 4 h. The 2N formulation reached compressive-strength values of up to 360 $\pm$ 25 MPa. These findings demonstrate the feasibility of processing high-solids nano-zirconia pastes by DIW and support further development of the approach for dental ceramic structures. Additional mechanical, dimensional, aging, and tribological characterization is required before conclusions can be drawn regarding the performance of DIW-fabricated zirconia restorations under clinical conditions.

Supplementary Materials: The following supporting information can be downloaded at: https://www.mdpi.com/article/10.3390/ceramics9100113/s1, Figure S1: Rietveld refinement of the XRD pattern of the 3YZrO_2-N powder.

Author Contributions: Conceptualization, I.K., E.R., and A.T.; methodology, P.A., E.R., P.G., M.P., O.A., S.K. and I.K.; validation, P.A., E.R., P.G. and I.K.; formal analysis, P.A., E.R., P.G., M.P., O.A., S.K. and I.K.; investigation, P.A., E.R., P.G., M.P., O.A., S.K. and I.K.; resources, A.T., D.T. and C.-D.A.; data curation, P.A., E.R. and I.K.; visualization, P.A. and I.K.; writing—original draft preparation, I.K. and P.A.; writing—review and editing, I.K., P.A., P.G., M.P., S.K., D.T. and A.T.; supervision, D.T., I.K., C.-D.A. and A.T.; project administration, D.T., I.K., C.-D.A. and A.T.; funding acquisition, C.-D.A., D.T. and A.T. Author Athena Tsetsekou passed away prior to the publication of this manuscript. All authors have read and agreed to the published version of the manuscript.

Funding: This research has been co-financed by European Regional Development Fund of the European Union and Greek national funds through the Operational Program Competitiveness, Entrepreneurship and Innovation, under the call RESEARCH—CREATE—INNOVATE (project code: T2EΔK-04124, 3DENT).

Data Availability Statement: The raw data supporting the conclusions of this article will be made available by the authors on request.

Conflicts of Interest: Author Constantina-Dia Andreouli was employed by the company Materials Industrial Research and Technology Center MIRTEC S.A. The remaining authors declare that the research was conducted in the absence of any commercial or financial relationships.

References

1. Saha, S.; Roy, S. Metallic Dental Implants Wear Mechanisms, Materials, and Manufacturing Processes: A Literature Review. *Materials* **2023**, *16*, 161. [CrossRef]
2. Sales, P.H.d.H.; Barros, A.W.P.; de Oliveira-Neto, O.B.; de Lima, F.J.C.; Carvalho, A.d.A.T.; Leão, J.C. Do zirconia dental implants present better clinical results than titanium dental implants? A systematic review and meta-analysis. *J. Stomatol. Oral Maxillofac. Surg.* **2023**, *124*, 101324. [CrossRef]

3. Spitznagel, F.A.; Balmer, M.; Wiedemeier, D.B.; Jung, R.E.; Gierthmuehlen, P.C. Clinical outcomes of all-ceramic single crowns and fixed dental prostheses supported by ceramic implants: A systematic review and meta-analyses. *Clin. Oral Implants Res.* **2022**, *33*, 1–20. [CrossRef]
4. Bapat, R.A.; Yang, H.J.; Chaubal, T.V.; Dharmadhikari, S.; Abdulla, A.M.; Arora, S.; Rawal, S.; Kesharwani, P. Review on synthesis, properties and multifarious therapeutic applications of nanostructured zirconia in dentistry. *RSC Adv.* **2022**, *12*, 12773–12793. [CrossRef]
5. Haugen, H.J.; Chen, H. Is There a Better Biomaterial for Dental Implants than Titanium?—A Review and Meta-Study Analysis. *J. Funct. Biomater.* **2022**, *13*, 46. [CrossRef]
6. Jurado, C.A.; Villalobos-Tinoco, J.; Watanabe, H.; Sanchez-Hernandez, R.; Tsujimoto, A. Novel translucent monolithic zirconia fixed restorations in the esthetic zone. *Clin. Case Rep.* **2022**, *10*, e05499. [CrossRef]
7. Manicone, P.F.; Rossi Iommetti, P.; Raffaelli, L. An overview of zirconia ceramics: Basic properties and clinical applications. *J. Dent.* **2007**, *35*, 819–826. [CrossRef]
8. Kongkiatkamon, S.; Rokaya, D.; Kengtanyakich, S.; Peampring, C. Current classification of zirconia in dentistry: An updated review. *PeerJ* **2023**, *11*, e15669. [CrossRef]
9. Nakai, H.; Inokoshi, M.; Nozaki, K.; Komatsu, K.; Kamijo, S.; Liu, H.; Shimizubata, M.; Minakuchi, S.; Van Meerbeek, B.; Vleugels, J.; et al. Additively manufactured zirconia for dental applications. *Materials* **2021**, *14*, 3694. [CrossRef]
10. Abualsaud, R.; Alalawi, H. Fit, Precision, and Trueness of 3D-Printed Zirconia Crowns Compared to Milled Counterparts. *Dent. J.* **2022**, *10*, 215. [CrossRef]
11. Refaie, A.; Fouda, A.; Bourauel, C.; Singer, L. Marginal gap and internal fit of 3D printed versus milled monolithic zirconia crowns. *BMC Oral Health* **2023**, *23*, 448. [CrossRef]
12. Ebert, J.; Özkol, E.; Zeichner, A.; Uibel, K.; Weiss, Ö.; Koops, U.; Telle, R.; Fischer, H. Direct inkjet printing of dental prostheses made of zirconia. *J. Dent. Res.* **2009**, *88*, 673–676. [CrossRef]
13. Zocca, A.; Colombo, P.; Gomes, C.M.; Günster, J. Additive Manufacturing of Ceramics: Issues, Potentialities, and Opportunities. *J. Am. Ceram. Soc.* **2015**, *98*, 1983–2001. [CrossRef]
14. Shi, Y.; Wang, W. 3D inkjet printing of the zirconia ceramic implanted teeth. *Mater. Lett.* **2020**, *261*, 127131. [CrossRef]
15. Punia, U.; Kaushik, A.; Garg, R.K.; Chhabra, D.; Sharma, A. 3D printable biomaterials for dental restoration: A systematic review. *Mater. Today Proc.* **2022**, *63*, 566–572. [CrossRef]
16. Branco, A.C.; Silva, R.; Jorge, H.; Santos, T.; Lorenz, K.; Polido, M.; Colaço, R.; Serro, A.P.; Figueiredo-Pina, C.G. Tribological performance of the pair human teeth vs 3D printed zirconia: An in vitro chewing simulation study. *J. Mech. Behav. Biomed. Mater.* **2020**, *110*, 103900, Correction in *J. Mech. Behav. Biomed. Mater.* **2023**, *147*, 106041.. [CrossRef]
17. Branco, A.C.; Silva, R.; Santos, T.; Jorge, H.; Rodrigues, A.R.; Fernandes, R.; Bandarra, S.; Barahona, I.; Matos, A.P.A.; Lorenz, K.; et al. Suitability of 3D printed pieces of nanocrystalline zirconia for dental applications. *Dent. Mater.* **2020**, *36*, 442–455, Correction in *Dent. Mater.* **2023**, *39*, 861.. [CrossRef]
18. Pillai, S.; Upadhyay, A.; Khayambashi, P.; Farooq, I.; Sabri, H.; Tarar, M.; Lee, K.T.; Harb, I.; Zhou, S.; Wang, Y.; et al. Dental 3d-printing: Transferring art from the laboratories to the clinics. *Polymers* **2021**, *13*, 157. [CrossRef]
19. Teegen, I.S.; Schadte, P.; Wille, S.; Adelung, R.; Siebert, L.; Kern, M. Comparison of properties and cost efficiency of zirconia processed by DIW printing, casting and CAD/CAM-milling. *Dent. Mater.* **2023**, *39*, 669–676. [CrossRef]
20. Rodrigues, I.; Guedes, M.; Olhero, S.; Chefdor, A.; Branco, A.C.; Leite, M.; Serro, A.P. Development of free binder zirconia-based pastes for the production of dental pieces by robocasting. *J. Manuf. Process.* **2020**, *57*, 1–9, Correction in *J. Manuf. Process.* **2023**, *102*, 416.. [CrossRef]
21. Mohammadi, M.; Becker, G.; Diener, S.; Tulliani, J.; Katsikis, N.; Palmero, P. Robocasting of dense zirconia parts using commercial yttria-stabilized zirconia granules and ultrafine particles. Paste preparation, printing, mechanical properties. *Ceram. Int.* **2022**, *48*, 1936–1946. [CrossRef]
22. dos Santos, C.; Baltazar, J.; Alves, M.F.R.P.; Olhero, S.M. Translucent zirconia dental prosthesis processed by Direct Ink Writing: Updates and challenges. *J. Manuf. Process.* **2024**, *131*, 1656–1666. [CrossRef]
23. Baltazar, J.; Fellipe, M.; Pais, R.; Martins, M.A.; Paula, M.; Torres, C.; Santos, C.; Olhero, S. Flexural strength of 3Y-TZP bioceramics obtained by direct write assembly as function of residual connected-porosity. *J. Mech. Behav. Biomed. Mater.* **2022**, *126*, 105035. [CrossRef]
24. Tyagi, B.; Sidhpuria, K.; Shaik, B.; Jasra, R.V. Synthesis of nanocrystalline zirconia using sol-gel and precipitation techniques. *Ind. Eng. Chem. Res.* **2006**, *45*, 8643–8650. [CrossRef]
25. *ASTM C20-00(2010)*; Standard Test Methods for Apparent Porosity, Water Absorption, Apparent Specific Gravity, and Bulk Density of Burned Refractory Brick and Shapes by Boiling Water. ASTM International: West Conshohocken, PA, USA, 2000; pp. 1–3. [CrossRef]
26. Uma Maheswari, A.; Mohan, S.R.; Saravana Kumar, S.; Sivakumar, M. Phase tuning of zirconia nanocrystals by varying the surfactant and alkaline mineralizer. *Ceram. Int.* **2014**, *40*, 6561–6568. [CrossRef]

27. Wang, J.; Zhang, B.; Chen, Y.; Wang, L.; Du, Y.; Wang, X. A comparison of the mechanical proprieties of different types of primary tooth restorations: An in vitro study. *Clin. Oral Investig.* **2022**, *26*, 4419–4426. [CrossRef]
28. Bennett, C.; Sojithamporn, P.; Thanakulwattana, W.; Wattanutchariya, W.; Leksakul, K.; Nakkiew, W.; Jantanasakulwong, K.; Rachtanapun, P.; Suhr, J.; Sawangrat, C. Optimization of 3D Printing Technology for Fabrication of Dental Crown Prototype Using Plastic Powder and Zirconia Materials. *Materials* **2022**, *15*, 8618. [CrossRef]
29. Willems, G.; Lambrechts, P.; Braem, M.; Vanherle, G. Composite resins in the 21st century. *Quintessence Int.* **1993**, *24*, 641–658.
30. Kocjan, A.; Logar, M.; Shen, Z. The agglomeration, coalescence and sliding of nanoparticles, leading to the rapid sintering of zirconia nanoceramics. *Sci. Rep.* **2017**, *7*, 2541. [CrossRef]
31. Muccillo, R.; Muccillo, E.N.S. An experimental setup for shrinkage evaluation during electric field-assisted flash sintering: Application to yttria-stabilized zirconia. *J. Eur. Ceram. Soc.* **2013**, *33*, 515–520. [CrossRef]
32. Li, W.; Ghazanfari, A.; McMillen, D.; Leu, M.C.; Hilmas, G.E.; Watts, J. Characterization of zirconia specimens fabricated by ceramic on-demand extrusion. *Ceram. Int.* **2018**, *44*, 12245–12252. [CrossRef]
33. Yu, T.; Zhang, Z.; Liu, Q.; Kuliiev, R.; Orlovskaya, N.; Wu, D. Extrusion-based additive manufacturing of yttria-partially-stabilized zirconia ceramics. *Ceram. Int.* **2020**, *46*, 5020–5027. [CrossRef]
34. Wang, L.; D'Alpino, P.H.P.; Lopes, L.G.; Pereira, J.C. Mechanical properties of dental restorative materials: Relative contribution of laboratory tests. *J. Appl. Oral Sci.* **2003**, *11*, 162–167. [CrossRef]
35. Buj-Corral, I.; Vidal, D.; Tejo-Otero, A.; Padilla, J.A.; Xuriguera, E.; Fenollosa-Artés, F. Characterization of 3d printed yttria-stabilized zirconia parts for use in prostheses. *Nanomaterials* **2021**, *11*, 2942. [CrossRef]
36. Frąckiewicz, W.; Królikowski, M.; Kwiatkowski, K.; Sobolewska, E.; Szymlet, P.; Tomasik, M. Comparison of Dental Zirconium Oxide Ceramics Produced Using Additive and Removal Technology for Prosthodontics and Restorative Dentistry—Strength and Surface Tests: An In Vitro Study. *Materials* **2024**, *17*, 168. [CrossRef]
37. Chun, K.J.; Lee, J.Y. Comparative study of mechanical properties of dental restorative materials and dental hard tissues in compressive loads. *J. Dent. Biomech.* **2014**, *5*, 1–6. [CrossRef]
38. Xia, X.; Wang, T.; Zhou, J. Effect of particle size distribution on properties of zirconia ceramics prepared by direct ink writing. *Mater. Res. Express* **2026**, *13*, 045401. [CrossRef]
39. Gomes, P.d.L.; Freitas, B.X.; Azoubel, R.A.; Alves, M.F.R.P.; Daguano, J.K.M.B.; dos Santos, C. Direct ink writing of 3Y-TZP ceramics using PEG-Laponite ® as additive. *Ceram. Int.* **2023**, *49*, 26348–26358. [CrossRef]

Disclaimer/Publisher's Note: The statements, opinions and data contained in all publications are solely those of the individual author(s) and contributor(s) and not of MDPI and/or the editor(s). MDPI and/or the editor(s) disclaim responsibility for any injury to people or property resulting from any ideas, methods, instructions or products referred to in the content.